UNDERSTANDING FLIGHT-TEST DATA WITH CFD ROTOR SIMULATIONS: AN APPLICATION CASE ON THE H175 HELICOPTER

E. Roca León, D. Desvigne & M. Embacher
Airbus Helicopters S.A.S.
Marseille-Provence International Airport, F-13725 Marignane cedex, France

Abstract

In this work, comparisons between flight test data and simulations for the H175 rotor in several flight conditions are proposed. The Computational Fluid Dynamics (CFD) analysis relies on isolated rotor models including different tab arrangements and elastic blades. URANS simulations are performed using the FLOWer solver and are coupled with the comprehensive analysis code CAMRADII, which provides the rotor CSD model and the helicopter trim. A loose-coupling method is applied by exchanging information between the CFD solver and the comprehensive code at each or after several full rotor revolutions until a converged trimmed solution is obtained. The flight test data includes blade control angles, sectional loads, control loads and damper loads allowing for an in-depth comparison between flight and simulations.

A full helicopter trim is performed using the comprehensive aeromechanics code HOST in order to extract fuselage attitudes and aerodynamic forces used subsequently as trim targets for the isolated rotor coupled CSD/CFD simulations with 3 degrees of freedom (DoF) trim. Predictive capabilities are thus dependent on accurate modelling of the fuselage drag and download in the initial full helicopter trim, in order to obtain rotor positions and control angles similar to those seen in flight.

A conventional (cruise) level flight as well as a high altitude level flight presenting dynamic stall have been simulated and analyzed with a focus on pitch link loads and inter-blade damper loads. Additional cases at higher load factors — namely turn manoeuvers at load factors 1.07g and 1.3g — are also presented.

1. INTRODUCTION

Extensive flight-testing is needed during the development of a rotor in order to confirm expected behavior, stability and to monitor loads and projected lifetime of critical parts. During this phase, the blades are tuned up depending on the observed rotor behavior at the limits of the flight envelope. Typically, the dynamics and stability of the blade can be improved by modifying the mass distribution and/or the blade tab settings and these modifications can be implemented relatively fast between flights. This process generates a wealth of data, which can be used to benchmark the available simulation methods and tools and assess their capability to blindly predict the observed phenomena. Conversely, when a good agreement with flight data is obtained the simulations can shed light on the physical mechanisms at play thanks to very detailed local information unavailable in flight. A distinction can thus be made with respect to the simulation objectives: aiming to blindly predict the flight data or trying to reproduce the flight by tuning the simulation parameters.

The simulation of helicopter rotors remains a multi-disciplinary complex topic given the variety of phenomena occurring in a single rotor revolution: transonic flow on the advancing blade, reversed flow and flow separation in the retreating blade, blade vortex interactions, elastic deformations and general unsteadiness. In the case of highly loaded rotors additional problems can appear, such as dynamic stall, which remains a modelling challenge for the CFD community.

In the last two decades, the simulation capabilities have greatly improved and notably the use CFD/CSD coupling has been proven essential to be in reasonable agreement with experimental airloads measurements. The UH-60A Black Hawk helicopter test campaign [1] provided a detailed benchmark for Bousman *et al.* [2] to investigate dynamic stall in a complete rotor and to Postdam *et al.* [3] to demonstrate the loose coupling strategy between CFD and a comprehensive rotor code with the objective of predicting the rotor airloads. The 7A rotor wind tunnel test campaign by ONERA constitutes another well-documented database providing a benchmark for simulation validation. Ortun *et al.* [4] performed loose coupling CFD/CSD simulations on a high-speed cruise case and a high-thrust case featuring dynamic stall. More recently, Richez [5] and Castells [6] performed additional simulations on dynamic stall cases of the 7A rotor; a good agreement with the experimental data was found in these simulations. Further work by Kowarsch [7] showcases the application of a 6DoF coupling strategy to the H145 helicopter, and more recently Letzgus [8] investigates dynamic stall in turn flight conditions with an application to the full *Bluecopter* demonstrator [9] using a 3DoF trim. The pitch-link loads were compared with flight-test data for a reasonable agreement albeit some phase shifts and a slight underprediction of the pitch-link load magnitude with respect to the measured levels.

In this work, a loose coupling methodology between CFD (namely DLR's code FLOWer [10]) and a rotorcraft comprehensive code (CAMRADII of Johnson Aeronautics [11]) is applied to isolated rotor simulations with the objective to reproduce flight test data in challenging flight conditions.

In order to achieve this goal the 3 DoF trim objectives of the high-fidelity simulations are tuned using flight data. This can be done using different means such as imposing the blade flapping and/or tuning a low-fidelity full helicopter comprehensive simulation so that major flight parameters are matched (e.g. rotor disk inclination). Rotor trim targets are thus obtained and used subsequently in the high-fidelity

Presented at 48th European Rotorcraft Forum, Winterthur, Switzerland, 6-8 September, 2022

simulations. Airbus Helicopters' in-house code HOST [12] is used for this step. The use of flight-test data aims to reduce the modeling gap caused by not including the fuselage and a full 6 DoF trim in the CFD/CSD coupling.

This procedure can be used to explore the effect of incremental changes on the blade design such as mass distribution and tab settings based on an initial simulation tuned with the help of flight data. The methodology is applied to a range of increasingly challenging flight conditions, standard cruise, high-thrust cruise with reduced rotor speed and stabilized turns with a load factor up to 1.3g allowing to reach conclusions regarding the proposed approach. The main focus of the comparison is on the control loads and the blade airloads.

2. GEOMETRIES AND INTERNAL STRUCTURE DESCRIPTION

2.1. Geometries

In this work, the five-bladed Spheriflex® H175 main rotor is considered. The H175 blade is a straight blade of radius R = 7.4m constructed from the OA312, OA309 & OA407 airfoils. The tip features an ONERA SPP8 parabolic design [13]. An overview of the blade is proposed in Figure 1.

Figure 1 – Overview of the certified H175 blade (incl. tabs)

The certified H175 blade shows two tabs implemented from the radial station 0.60R to 0.90R. A first tracking tab with a chord of 20mm is introduced within the span range 0.60R to 0.71R. The tab slope angle is fixed to 0°. A second tab with a chord of 44mm is then implemented spanwise within the range 0.71R to 0.90R. The tab slope angle is adjustable, as illustrated in Figure 2. A detailed view of the H175 blade installed tabs is proposed in Figure 3.

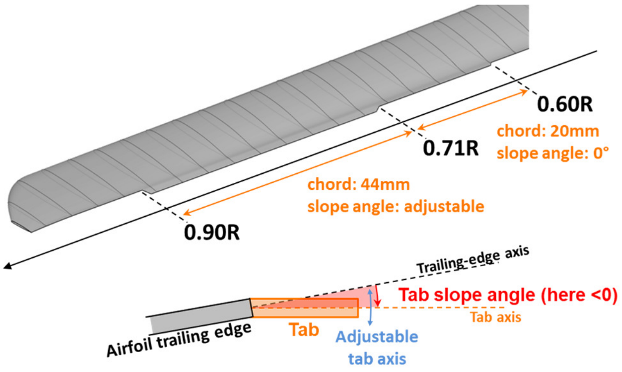

Figure 2 – Characteristics of the H175 blade tab arrangement

Figure 3 – Magnified view of the H175 blade tabs

We consider in what follows a tab slope angle of -8° (i.e. trailing edge to the bottom as measured from the trailing-edge axis, cf. Figure 2) as reference, corresponding to the tab settings of the certified blade. A tab slope angle of 0° has also been considered in this work.

2.2. Internal structure

The baseline blade internal structure considered in this work is the one defined in the blade predesign phase and includes the reference stiffness-, mass- and inertia-distribution along the blade span. The certified (serial) version of the blade includes two major changes with respect to the baseline reference:

- ✓ a concentrated mass of 2kg located at the radial station 0.70R ;
- ✓ an additional linear mass of 2.5kg along the blade leading edge.

2.3. List of blade configurations

Four different blade configurations have been considered in this work. Those differ in terms of the tab angular settings and the internal blade structure. Those configurations are summarized in Table 1.

Conf ID	tab settings	Internal structure
NOTAB_BSL	No tabs	baseline
TAB8_BSL	-8°	baseline
TAB0_SER	0°	serial
TAB8_SER	-8°	serial

Table 1 – List of configurations

3. FLIGHT CONDITIONS

Several flight conditions have been considered, as summarized in Table 2. Those include a standard level flight with moderate rotor loading, as well as a high-altitude level flight with a reduced rotor rotational speed that showed dynamic stall in flight for the serial blade with unbent tabs. Several high-altitude coordinated turns characterized by a load factor of 1.3g are also at focus in this work. For the blade configuration with no tabs, a turn with a load factor reduced to 1.07g has also been considered.

4. NUMERICAL PROCEDURE

The proposed approach is based on an initial full helicopter 6 DoF trim performed with Airbus Helicopters' in-house comprehensive rotor simulation code HOST [12] which is tuned to match flight test data. This trim yields trim targets that are subsequently used in the high-fidelity simulations.

.

CASE ID	CONF ID	NR [%]	ΔISA [°C]	Zp [ft]	TAS [kt]	N [%g]	H/C mass [kg]	FT data available?
LEVEL_REF_SER	TAB8_SER	105%	+4	5720	144	1.00	7550	✓
LEVEL_REF0_SER	TAB0_SER	100%	+7	10180	137	1.00	7500	✓
TURN_1.07G_NOTAB	NOTAB_BSL	105%	+10	9820	149	1.07	7310	✓
TURN_1.3G_NOTAB	NOTAB_BSL	105%	+10	9875	140	1.30	7350	✗
TURN_1.3G_REF_BSL	TAB8_BSL	105%	+10	9875	140	1.30	7350	✗
TURN_1.3G_REF_SER	TAB8_SER	105%	+10	9875	140	1.30	7350	✓

Table 2 – List of flight conditions

The use of flight test data to correct the HOST trim intends to provide a better agreement with the experimental data and to compensate for the fact that only 3 DoFs are taken into account in the coupling process.

4.1. HOST pre-trim

The three trim targets for the isolated rotor simulations presented in the following have been obtained by precursor simulations with the HOST code, as for this latter code a complete helicopter model of the H175 has been available. The complete helicopter model comprises the fuselage aerodynamics and allows for a 6-DoF trim (a so-called free flight trim), from which three rotor quantities can be selected as trim targets for subsequent use in the isolated rotor simulation with CFD/CSD coupling.

The approach in this basic form hence is entirely predictive, as no flight test data, such as measured attitudes, mast moments or thrust targets, is involved. Depending on the choice of the kind of rotor loads to be carried over to CFD/CSD simulations, forces or moments, the representativeness of the CFD simulation is impacted. The HOST result will not in general provide a rotor solution where the force component in the rotor disk plane (H-force) is correct. Hence, even if the fuselage aerodynamic polar was perfectly realistic, depending on the rotor control power, a deviation in pitch attitude is obtained, which is carried over to the CFD isolated rotor simulation.

Tip-path plane orientation in space of the CFD/CSD simulations will then depend on the kind of rotor load targets selected. If the rotor forces vector is chosen and the airframe drag gradient with respect to shaft incidence (*i.e.* $d(D_{Fus})/d\alpha$) is moderate, an improved prediction of the H-force by CFD will bring the rotor tip-path plane back towards the real incidence, but at the expense of an offset in flapping and control axis inclination relative to the shaft.

Depending on the simulation task, either a realistic incidence of the rotor disk may be of high importance, or a particularly high fidelity in blade-root flapping might be sought. The former certainly is the case if rotor performance is at focus, while the latter strategy can help to model dynamic behaviour, especially with rotors of bearingless or hingeless design, and blade structural characteristics that couple elastic pitch and flap motions.

The interblade damper used on the H175 is characterized by many geometric non-linearities; damper motion depends on blade root lag, flap, and pitch, whereby the non-linearities produce, for instance, higher-harmonics in dependence of the amount of collective pitch. In this case, both a realistic collective, i.e. control axis incidence, and cyclic controls, as well as correct flapping with respect to the shaft are required, and the choice of the trim targets based on the generally imperfect prediction of a comprehensive code is a difficult task.

Because the simulation of damper behaviour was one of the objectives of the “high load cruise” simulation (ID: LEVEL_REF0_SER, cf. Table 2), and since for this flight blade-root motion had been measured with wire potentiometers, it was decided to re-trim towards the measured flap angles β_{1C}, β_{1S} (longitudinal and lateral flap angles respectively). In addition, the pitch attitude Θ measured in flight was prescribed. Extensive calibration of the wire potentiometer method on ground, and cross-checking with the mast moments in flight, took place. It therefore was hoped that flap angles were reconstructed sufficiently precisely, such that, if the elastic flap motions are simulated with good fidelity, the tip-path plane incidence is properly reproduced even though no propulsive force target was given. A precursor simulation with HOST was carried out as well to provide the main rotor thrust target T_{MR}. The trim laws employed are listed in Table 3 under “Cruise reproductive”.

For the standard cruise (ID: LEVEL_REF_SER, cf. Table 2), a purely predictive trim strategy was employed, targeting the HOST-predicted rotor thrust and in-plane forces T_{MR}, Fx, Fy (for main rotor thrust, in-plane longitudinal and lateral H-force components). The laws termed “Cruise Predictive” in Table 3 are used, prescribing the HOST pitch and roll attitudes Θ, Φ in the CFD/CSD setup.

For the turn flights (IDs: TURN_1.07G_NOTAB and TURN_1.3G_REF_SER, cf. Table 2), the generation of trim targets did also rely entirely on the HOST prediction. Similar to a flight-test practice, the collective COLL was to be kept at a corresponding level flight setting, with the vertical speed V_Z as a free variable. Therefore, a level flight was calculated in HOST in first instance, in order to obtain the collective setting, and using rotor forces as targets a CFD/CSD simulation was added in order to refine the collective (“Cruise predictive” law in Table 3).

In a second step, a coordinated turn flight to the right at prescribed load factor and level flight collective, and with the descent rate V_Z as a free variable, was simulated in HOST to obtain the rotor force trim targets (T_{MR}; Fx; Fy) for the CFD/CSD simulations. Total flight speed V is prescribed, and the slope $\tau = \tan^{-1}(V_Z/V_H)$ (with V_H being the horizontal speed) ensures the drag/propulsion equilibrium, whereby the demand of thrust determines largely the no-feathering plane incidence. The load factor of 1.3g is covered by the demand for global load balance ($\Sigma F = 0$, $\Sigma M = 0$), while the coordinated turn is synonymous to zero lateral acceleration Ny in the helicopter system. Although the requirement is of geometric nature and leaves 2 DoFs for the orientation of the helicopter, a target Ny = 0 was included into the trim law and all three of the attitude angles ψ, Θ, Φ (yaw, pitch, roll) were liberated. The CSD code was set up to vary the main rotor cyclic control angles LATCYC and LONGCYC (lateral and longitudinal cyclic rotor angles) and the shaft incidence α, cf. Table 3.

	HOST		**CFD/CSD**	
Case	**Trim DoFs**	**Trim Targets**	**Trim DoFs**	**Trim Targets**
Cruise reprod.	COLL LNGCYC LATCYC $COLL_{TR}$ Θ Φ	ΣF = 0 ΣM = 0	COLL LNGCYC LATCYC	T_{MR} β_{1C} β_{1S}
Cruise predict.	COLL LNGCYC LATCYC $COLL_{TR}$ Θ Φ	ΣF = 0 ΣM = 0	COLL LNGCYC LATCYC	T_{MR} Fx Fy
Turns	COLL LNGCYC LATCYC $COLL_{TR}$ ψ Θ Φ V_H V_Z	ΣF = 0 ΣM = 0 V Ny = 0	α LNGCYC LATCYC	T_{MR} Fx Fy

Table 3 – Trim law strategy

In particular, it was chosen to test a set up corresponding rather to a steady wind-tunnel situation. This means a departure from the flight dynamics of a turn: The pitch rate *q* about the lateral axis (in helicopter system) is not present. In a turn, the rotor disk needs to be re-oriented at this pitch rate, which requires extra lift at the advancing blades, and a lift reduction on the retreating blades. Consequently, longitudinal cyclic needs to be slightly increased. A side effect is also the modification of the rotor drag in disk plane. Furthermore, aerodynamic damping requires an adjustment of lateral cyclic. These three effects are not modelled by the simplified set up. Estimating them in HOST shows that, for the pitch rate *q* = 4.1deg/s as in the 1.3g case, their impact remains in the order of ΔLNGCYC = +0.22°, ΔLATCYC = -0.18° and $\Delta\beta_{1C}$ = -0.48° (i.e. forward disk tilt) when trimming for same rotor forces.

4.2. CAMRADII/FLOWer re-trim

For the re-trim activities considering an isolated rotor, the rotorcraft comprehensive code CAMRADII of Johnson Aeronautics [11] has been used for the Flight Dynamics (FD)/Computational Structure Dynamics (CSD) aspects, along with the CFD code FLOWer developed by the German Aerospace Center (DLR) [10].

A loose CFD/CSD coupling approach has been adopted, which basically consists in replacing iteratively the low-fidelity aerodynamic loads obtained by CAMRADII from 2D steady airfoil polars by the high-fidelity aerodynamic rotor-blade loads computed by CFD (FLOWer), as comprehensively described in [7]. CAMRADII and FLOWer have been preferred to other available tools such as HOST/elsA coupling [6] or HOST/FLOWer coupling [14], because they constitute the most mature toolchain in CFD/CSD coupling in use at Airbus Helicopters (AH).

4.2.1. CSD solver

CAMRADII includes multibody dynamics, nonlinear finite elements, structural dynamics, and low-fidelity rotorcraft aerodynamics relying on steady 2D airfoil polars. The structural rotor blade dynamics, blade deformation and rotor control angles and/or attitudes that are required to trim the rotor in regards of target rotor loads are typical outputs of a CAMRADII run.

CAMRADII is used in a 3DoF approach using different parameters depending on the flight case considered The parameters are chosen according to Table 3.

In the current work, the structure dynamics solution is sought using a Newton-Raphson algorithm considering 10 blade modes with 10 harmonics for all CAMRADII output quantities, taking into account 30 rotor azimuthal positions per revolution.

4.2.2. CSD model

The CAMRADII model of the H175 Spheriflex® rotor is based on an adaptation of the HOST H175 model extensively used at AH. The major challenge lies in the modelling of the interblade lead-lag dampers of the Spheriflex® articulated rotor hub, because the standard process of modelling blade dampers in CAMRADII — which consists in assigning for each blade stiffness and damping properties to the blade articulation joint degrees of freedom — can hardly be used.

The five-bladed main rotor model is implemented as a single load path model with swashplate control mechanism rotating clockwise and without tabs as baseline. The spherical bearing is represented by a lag-flap hinge followed by a pitch bearing at position 0.290 m. The main rotor model incorporates pre-cone and pre-sweep angles realized in the spherical bearings. The CAMRADII modelling approach consists in defining the rotor geometry without cone and sweep angle and introducing pre-coning and pre-sweeping by offsets in the spherical bearing lag and flap joint definitions. Thus, the rigid rotor model configuration used as reference geometry for mesh deformation in the CFD-CSD coupling tool chain is based on the blades aligned to the radial direction.

For the baseline rotor model (without interblade damper modelling), the backbone of the structural model consists of 16 finite beam elements with typically two elastic degrees of freedom in flap, lag, torsion and axial motions. The integration of stiffness and mass matrices of the beam elements is performed by Gauss integration using 20 stations distributed along the beam element according to the Gaussian integration scheme. The two inboard elements do not have elastic degrees of freedom representing the rigid rotor hub and the spherical bearing (with zero beam length). Aerodynamic discretization of the blade lifting line is based on 23 panels in the spanwise direction. The definition starts with the first panel inboard edge at 0.243R based on the airfoil tables available and the related airfoil distribution in spanwise direction. The panel distribution has been adapted so that tab edges and panel edges match, as shown in Figure 9.

An overview of the complete main-rotor model is proposed in Figure 4.

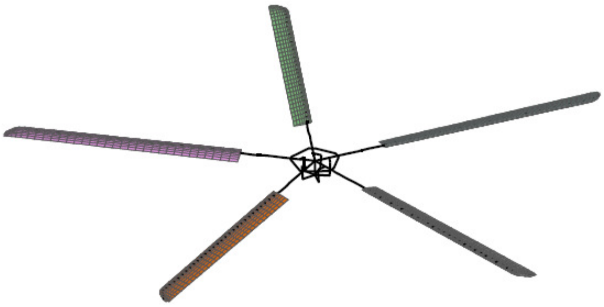

Figure 4 – Main rotor model featuring interblade damper components

CAMRADII offers the possibility to define swashplate control by means of the multibody formalism. Using this option, pitch horn, pitch link and rotating and non-rotating parts of the swashplate are connected by joints for adequate kinematics. Figure 5 presents the arrangement of these elements. Pitch horn and pitch link are plotted as lines while the rotating part of the swashplate is visualized by the five armed star. This star has three different degrees of freedom – translation in direction of the rotor shaft and out-of-plane tilting in both directions – and is linked to the lower part of the five pitch links of the five bladed rotor by joints. The upper part of each pitch link is attached to its corresponding pitch horn in order to introduce blade pitch motions into the blade when moved. Thus, blade pitch control is modelled in a quite realistic manner intrinsically considering pitch-flap and pitch-lag coupling and different control stiffness characteristics of collective, cyclic and reactionless control. The current models feature locked control flexibility i.e. high stiffness values are assigned in a quasi-static manner to swashplate and pitch link joints.

Interblade lead-lag dampers of the Spheriflex® rotor hub are modelled as rigid body components with joint degrees of freedom. Advantage is to have an adequate kinematic damper model automatically considering the rotor modes in the right manner by mechanical load paths. Geometric non-linearities leading to damper deflections at higher harmonics of the blade root motions are represented accurately. Main drawback is the need to solve the equations of motion for all blades simultaneously thus increasing significantly the computation time due to the large number of degrees of freedom. Furthermore, numerical conditioning tends to degrade due to larger size of the system matrices.

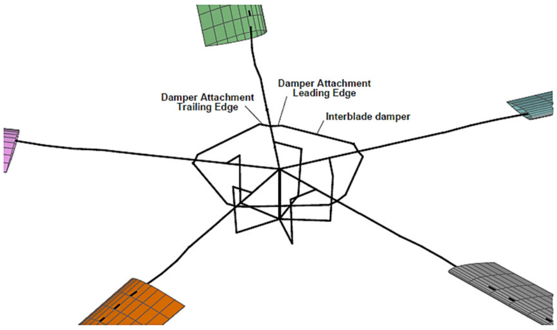

Figure 5 – Interblade damper model

4.2.3. CFD solver

The aerodynamic blade loads are evaluated using the finite-volume block-structured Reynolds-averaged Navier-Stokes (RANS) CFD code FLOWer. These high-fidelity loads are then used in replacement of the low-fidelity aerodynamic blade loads of CAMRADII. The RANS equations have been closed using the Shear Stress Transport k-ω variant of Menter's model [16]. A 5-stage Runge-Kutta central scheme with artificial dissipation has been used to evaluate numerically the Eulerian terms. The time-dependent URANS solution is obtained by integrating the governing equations using an implicit dual time-stepping approach developed by Jameson [16]. The ROT extension of FLOWer has been activated in order to calculate the unsteady flow around the moving and deforming blades.

All the FLOWer simulations have been performed over one complete rotor revolution, i.e. for a reference blade azimuth ψ varing from 0° (back blade) to 360°. The time step has been chosen so as to ensure an azimuthal step of 1° at considered rotor rotational speed during the convergence process. Blade elastic deformations as predicted by CAMRADII are taken into account in the CFD simulations thanks to the mesh-deformation technique.

4.2.4. CFD model

Multiblock grids of the different blade geometries have been employed. Each blade grid is composed of 64 blocks and 5.9M of nodes. A total of 249 radial stations have been considered in the spanwise direction, including 45 stations to represent the blade root. The body grid extrusion in the wall normal direction is around 1.5 blade chord length. In order to use the same block topology for all the geometries (with or without tabs), a small triangular junction has been considered at the tab edges.

The block topology and resulting structured grid are illustrated in Figure 6 and Figure 7 for the H175 blade with -8°–oriented tabs.

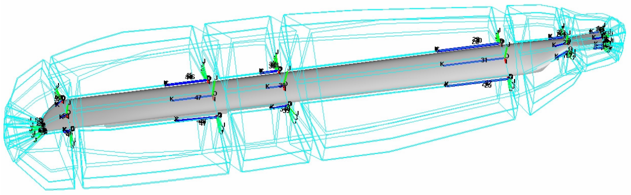

Figure 6 – Overview of the blade block topology (in cyan) of the H175 blade incl. tabs

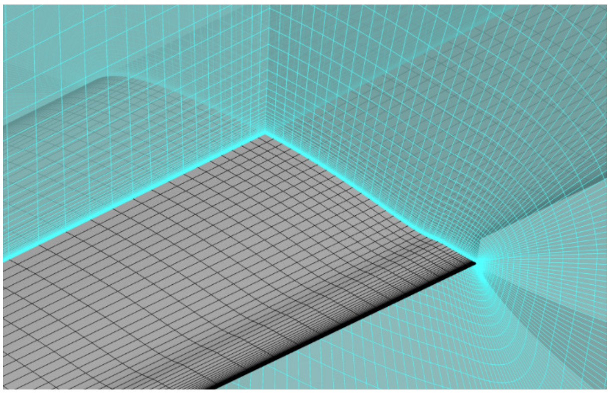

Figure 7 – Overview of the blade-skin grid (in grey) and the volume grid (in cyan) of the H175 blade incl. tabs

All the blade grids are then embedded into a background mesh of 20 rotor-diameter long in each direction with a prescribed motion and a prescribed deformation along the flap, pitch and lag axes according to the CAMRADII trim solution. A bi-directional transfer of the flow solution between the grids is ensured using a second-order Chimera interpolation technique at the grid overlapping boundaries [14]. The background mesh has been built using the Octree technique so as to ensure the smallest grid cell size where blades operate, while keeping the number of nodes reasonable. A grid resolution of 3 cm has thus been applied around the rotor disc area, which corresponds to the cell size at the outer boundaries of the blade grids where the flow data transfer is performed. Proceeding so ensures a low dissipative transport of the vortex structures between all the grids and a limited aliasing in the disturbances during the solution interpolations. The resulting background grid is composed of 1490 blocks and around 66M of nodes. An overview of the background grid with embedded blade grids is proposed in Figure 8.

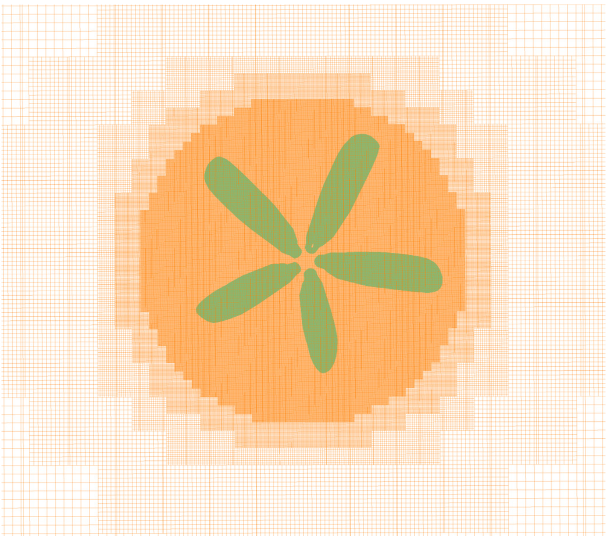

Figure 8 – Overview of the background grid (in orange) with successive Octree grid coarsening and embedded blade grids (in cyan)

4.2.5. CSD/CFD trim procedure

The loose coupling methodology is characterized by the application of a CFD-based load correction term on comprehensive code side. The so-called delta airloads term is updated sequentially at each iteration of the coupled cycle. Along with the convergence of the coupled cycle, the changes in the delta airloads term become smaller and smaller. After the changes have fallen below a user-defined threshold, the delta airloads can be considered as constant. At the same time the 2D steady polar based internal aerodynamic loads of the comprehensive codes have been completely replaced with the CFD loads and the comprehensive code's trim will be solely based on the CFD loads.

Each coupling cycle involves four steps which are sequentially executed as follows:

- ✓ Execute CAMRADII run to get the trim;
- ✓ Prepare position sensor data for FLOWer, incl. motion & blade deformation;
- ✓ Execute FLOWer computation to get the aerodynamic loads as a function of the blade azimuth;
- ✓ Prepare the delta airloads from the FLOWer sensors (blade-skin grid nodes) to the CII sensors (panels) for the next CAMRADII re-trim.

The preparation of the delta airloads is a critical step that implies the definition of a mapping between the radial stations of the CFD blade-skin grid and the CII panels, as illustrated in Figure 9 and Figure 10.

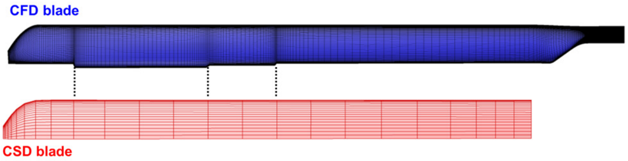

Figure 9 – Overview of mapping between the CFD sensors (radial stations of the blade-skin grid) and the CAMRADII panels

A special treatment has been applied for the aerodynamic loads at the blade root of the FLOWer grid. Indeed a part of the blade root is included in the CFD blade grid, i.e. the blade surface extends beyond the innermost airfoil section featuring the well-defined airfoil OA312, whereas on CAMRADII side, however, aerodynamic panels are only defined from the first aerodynamic section of the blade. As the innermost CAMRADII aerodynamic panel must be located within this profiled blade area (for which airfoil aerodynamic tables are available), the most inboard sequence of FLOWer sensors can be assigned to the first CAMRADII aerodynamic panel, as shown in Figure 10.

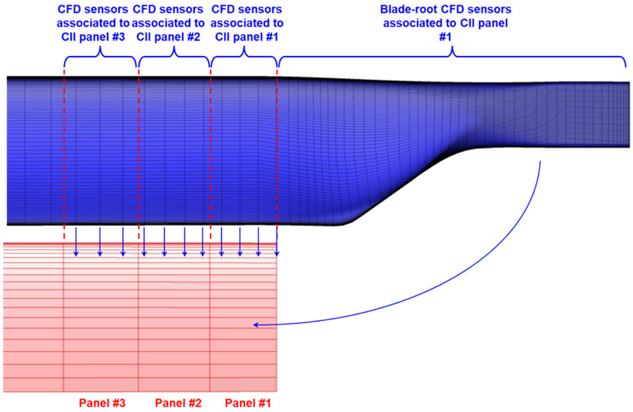

Figure 10 – Mapping between the CFD sensors (radial stations of the blade-skin grid) and the CAMRADII panels, and assigment of the CFD aerodynamic loads at the blade root to the innermost CAMRADII panel

For blade configurations with tabs, the preparation of the delta airloads also implies to prescribe the quarter-chord line on which the sectional aerodynamic moments are computed, as no tabs are included in the CSD model. The prescribed quarter-chord line thus corresponds to the quarter-chord line of the H175 blade without any tabs. This is illustrated in Figure 12.

The overall procedure for trim is illustrated in Figure 11. Depending on the flight case, trim convergence is achieved after six (level flight) to fifteen (turn at high load factor) trim iterations with a residual of the control angles or pitch between two successive iterations below 0.05°.

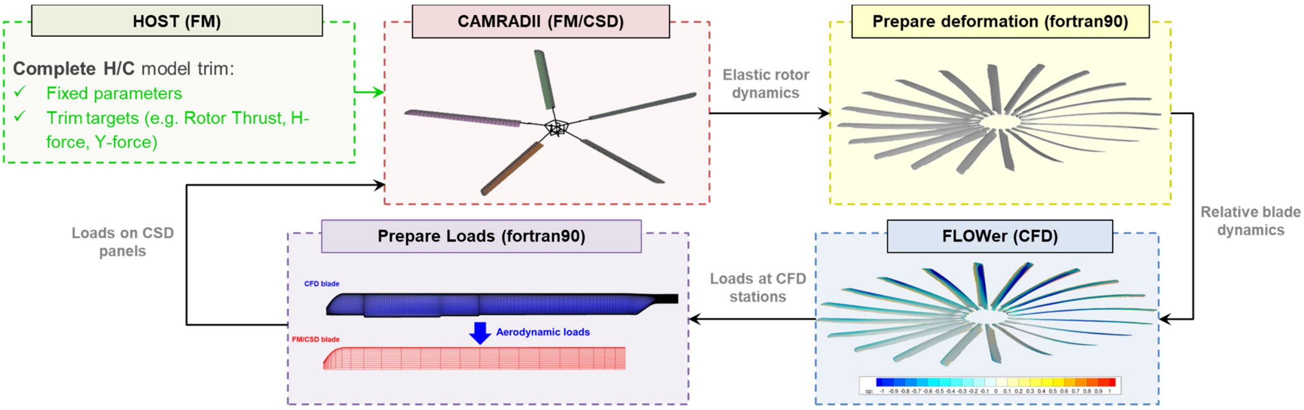

Figure 11 – Overall procedure for trim

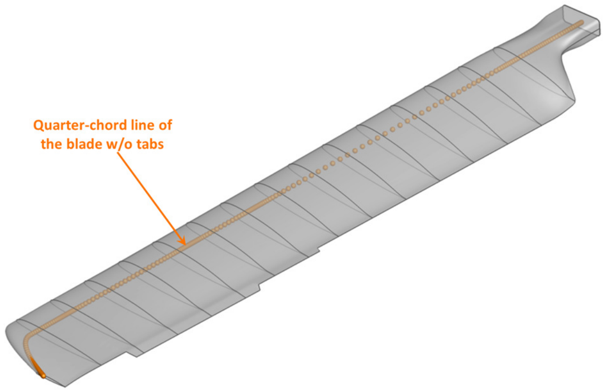

Figure 12 – Prescribed quarter-chord line of the blade without tabs for blade configurations with tabs

5. RESULTS

The simulation results of all the tested configurations are presented in this section. The chosen azimuth convention is 0° for the back blade (aligned with the tail boom), 90° for the advancing blade, 180° for the front blade and 270° for the retreating blade.

5.1. Level flights

5.1.1. Standard cruise

The first flight condition is a standard cruise point at 144kt and NR 105% at a pressure altitude of 5.7kft. The trim targets in the coupled simulation are the rotor thrust and the two in-plane forces out of the HOST pre-trim.

The resulting control angles along with the measured ones are presented in Table 4. A slight underprediction of the lateral cyclic angles might be partly explained by the absence of the flow disturbance by fuselage in the simulation.

The pitch-link load comparison with flight test data is presented in Figure 13 along with the corresponding harmonic decomposition in Figure 14. An excellent agreement is found between simulation and experiments including in absolute value, even if the simulations underpredict the higher-frequencies load amplitudes for the 2/rev and 5/rev components.

Variable	Simulation	Flight Data
COLL	5.23°	6.51°
LNGCYC	-6.13°	-6.48°
LATCYC	2.50°	3.53°

Table 4 – Trim control angles for LEVEL_REF_SER

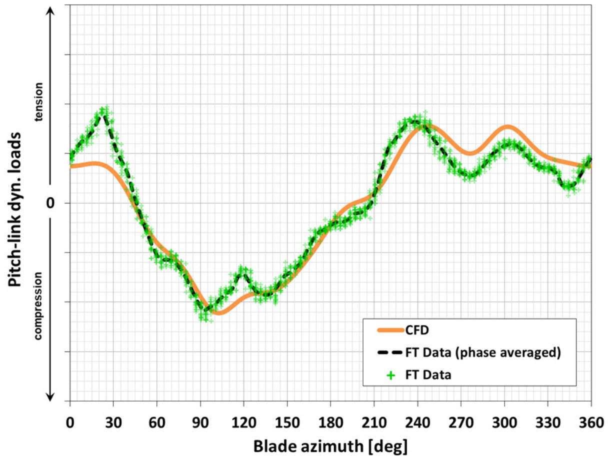

Figure 13 – Dynamic loads at pitch link as a function of the blade azimuth ψ for LEVEL_REF_SER

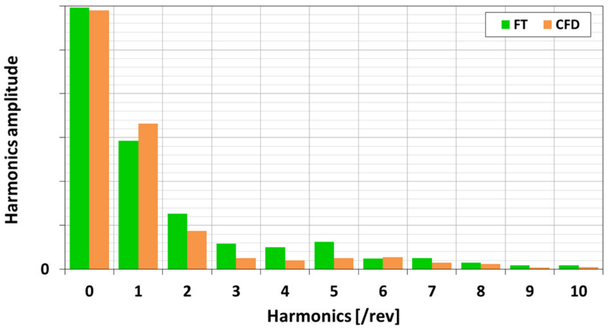

Figure 14 – Dynamic-loads harmonic decomposition (*i*/rev) at pitch link for LEVEL_REF_SER

5.1.2. High-load cruise

The second flight condition is a high-load cruise point at 137kt with slowed rotor speed (NR 100%) and tabs set to 0°, at a pressure altitude of 10kft. As the flapping angles were measured in flight in this case, the trim targets in the coupled simulation are the flapping angles and the rotor thrust**.**

The rotor control angles, summarized in Table 5 show non-negligible deviations from the flight test. A clear conclusion could not be reached, but a possible explanation is an offset in the measured fuselage angle-of-attack of the flight test, which, by prescribing the measured flapping, also determines the rotor disk inclination in the simulation. Reduced incidence in the simulation would induce an increase of the collective, and a need for more forward cyclic. It was also noted that the propulsive force obtained in the CFD/CSD simulation currently is too weak, which supports this notion.

Variable	Simulation	Flight Data
COLL	5.84°	6.70°
LNGCYC	-8.63°	-10.40°
LATCYC	4.47°	3.11°

Table 5 – Trim control angles for LEVEL_REF0_SER

For this case pitch-link loads show an increased dynamic behaviour suggesting the presence of dynamic stall (identified by high 6/rev component).

The pitch-link loads presented in Figure 15 and Figure 16 display a good agreement with flight data, especially the peak-to-peak amplitudes and the phase of the peaks at 330° and 25° suggest that the blade torsion behaviour is well captured. As expected, the tab setting at 0° greatly reduces the mean nose-down pitching moment (Figure 16 and Figure 14 share the same scales, mean value for the static component can thus be directly compared) unloading the rotor.

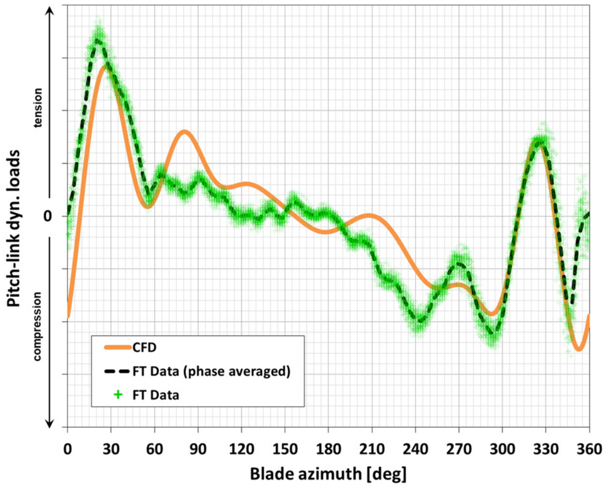

Figure 15 – Dynamic loads at pitch link as a function of the blade azimuth ψ for LEVEL_REF0_SER

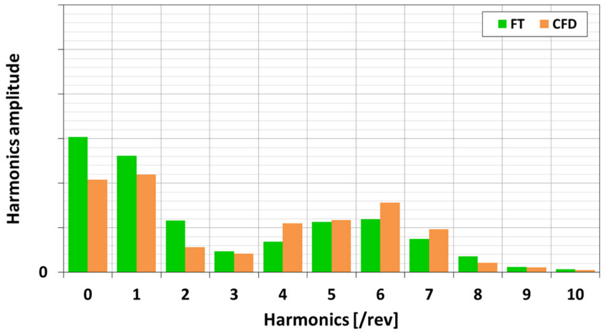

Figure 16 – Dynamic-loads harmonic decomposition (i/rev) at pitch link for LEVEL_REF0_SER

The simulated blade torsion (only the elastic part) is pictured in Figure 18 (right) and the torsion lobes at 6/rev are visible. The intensity of the elastic deformation correlates well with the pitch-link loads and seems to be caused by the stall phenomena starting in the 3rd quadrant of the rotor disk with trailing edge flow separation as shown in the skin friction coefficient shown in Figure 18 (left). The pattern of pitching moment stall in this zone (see Figure 17) caused by the flow separation seems to indicate the presence of dynamic stall.

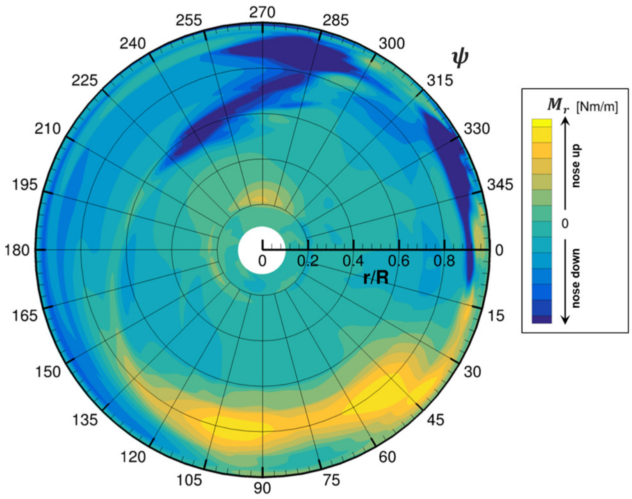

Figure 17 – Sectional pitching moment at the blade pitch axis as a function of the blade azimuth ψ for LEVEL_REF0_SER

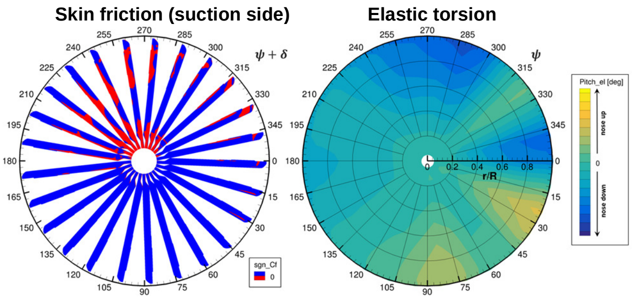

Figure 18 – Sign of the friction coefficient (blue: attached flow; red: separated flow) at the blade skin and blade elastic torsion as a function of the blade azimuth ψ for LEVEL_REF0_SER; δ is the blade lead lag angle

In addition to wire sensors measuring the rotor sleeve angles, flight instrumentation included strain gauges at seven radial stations measuring among other quantities the integrated torsion moment from the blade tip to the gauge station. The comparison between simulation and flight data of the integrated pitching moment is shown in Figure 19 for two radial stations (r/R=0.40 and r/R=0.95). A good agreement is obtained in absolute and peak-to-peak magnitudes. Harmonic content is truncated at 10 harmonics in the CAMRADII simulations which does not allow to capture higher frequency oscillations of the pitching moment at azimuths 330-30°.

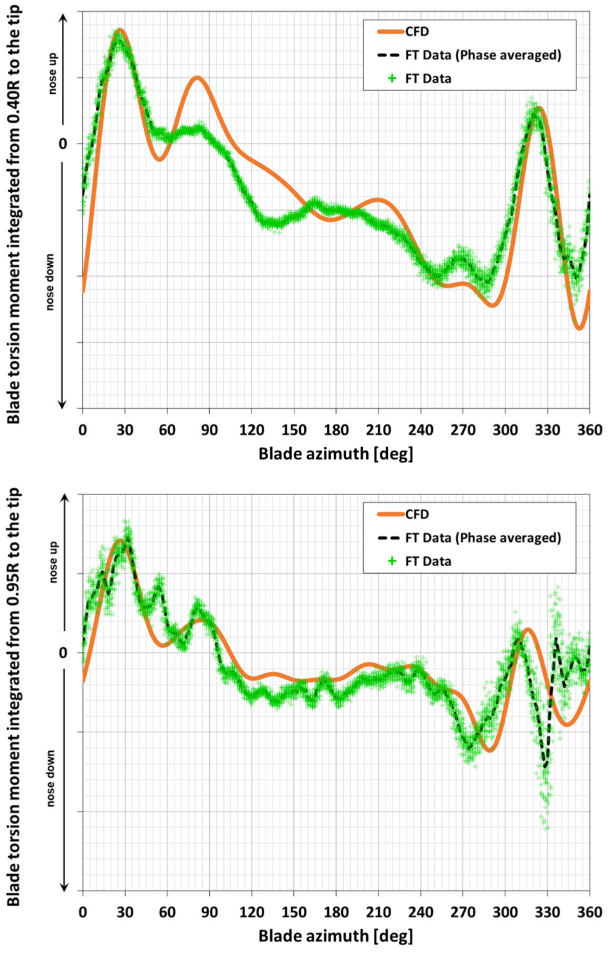

Figure 19 – Integrated pitching moment (positive for nose-up moment) at r/R=0.40 (top) and r/R=0.95 (bottom) for LEVEL_REF0_SER

A visualization of the flow field with a Q-criterion iso-surface coloured by the turbulent viscosity ratio is presented in Figure 20. The stall vortices have a higher turbulent viscosity than the tip vortices. A trailing-edge stall vortex is visible on the retreating blade, developing outboard. The back blade shows a separated region near the blade tip which might be shock induced as suggested by Richez in his analysis of a high-load cruise computation of the 7A rotor [5]. The H175 simulation shows overall qualitatively similar phenomena for this particular case.

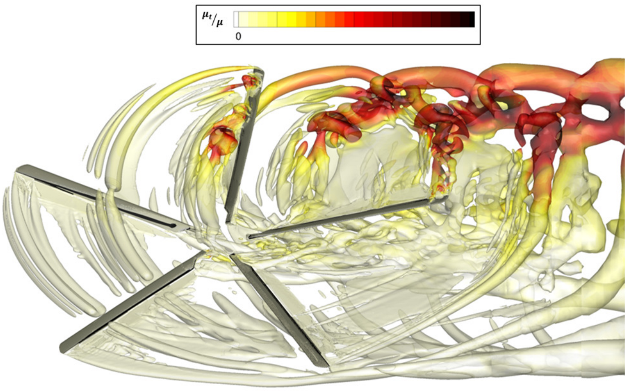

Figure 20 – Q-criterion iso-surface (Q = 25 rad²/s²) colored by the turbulent viscosity ratio μ/μₜ for LEVEL_REF0_SER

Finally, a comparison of the measured damper dynamic loads is presented in Figure 21. The damper peak-to-peak loads and the harmonic content seem to be reasonably well-predicted (cf. Figure 22), differences can be explained by the differences in the rotor control angles which in turn modify the distances between inter-blade damper attachments. Blade flapping was guaranteed by the trim approach, but the excitation of damper motion by cyclic pitching (in combination with the vertical offset of the damper attachments) is not completely reproduced. However the overall trends are satisfactory considering the complexity of the simulated case.

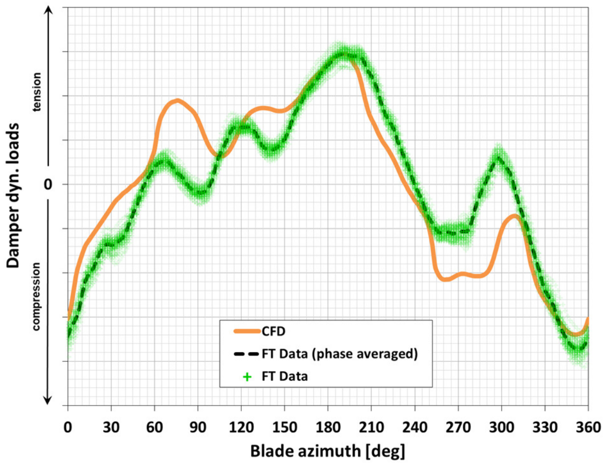

Figure 21 – Inter-blade damper loads as a the blade azimuth *ψ* for LEVEL_REF0_SER

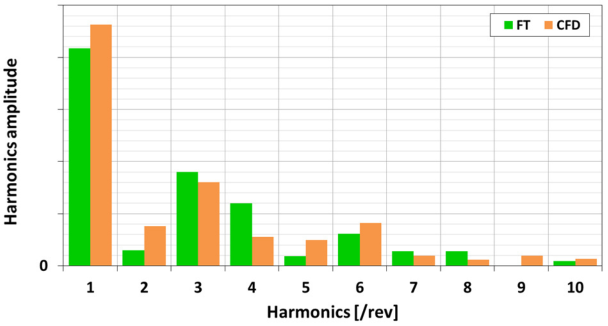

Figure 22 – Harmonic decomposition of the inter-blade damper loads (*i*/rev) for LEVEL_REF0_SER

5.2 Stabilized turns

5.2.1 Coordinated 1.07G turn: blade without tabs

This case represents a coordinated right turn with a banking angle of 20° initiated from cruise conditions. As explained in previous sections, a preliminary cruise computation was performed to obtain the collective control angles and subsequently during the turn the collective value was frozen and the pitch attitude freed in order to obtain the target load factor.

Variable	Simulation	Flight Data
COLL	4.14°	5.51°
LNGCYC	-8.39°	-8.7°
LATCYC	2.03°	2.5°
AoA	1.18°	1.59°

Table 6 – Trim control angles for TURN_1.07G_NOTAB

Results regarding the dynamic loads at the pitch link are illustrated in Figure 23 for the variations with regards to blade azimuthal position and Figure 24 for the harmonic aspects. They show quite similar trends as in high-load cruise with tabs set at 0°. A comparable underestimation by CFD of the static-and-1/rev component is also observed. A deeper analysis of other variables is not warranted for the sake of brevity, as it would show similar trends as in high load cruise with tabs set at 0°.

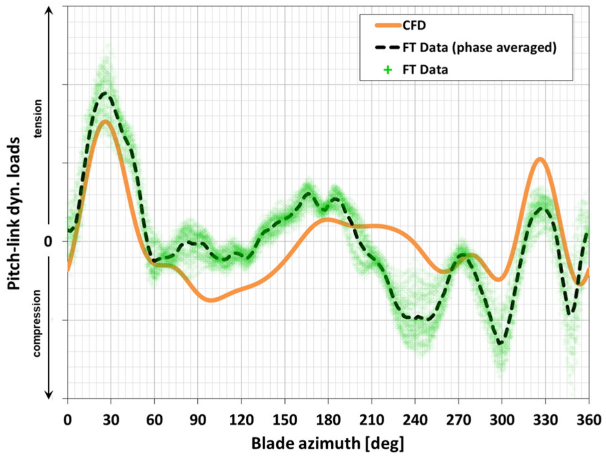

Figure 23 – Dynamic loads at pitch link as a function of the blade azimuth ψ for TURN_1.07G_NOTAB

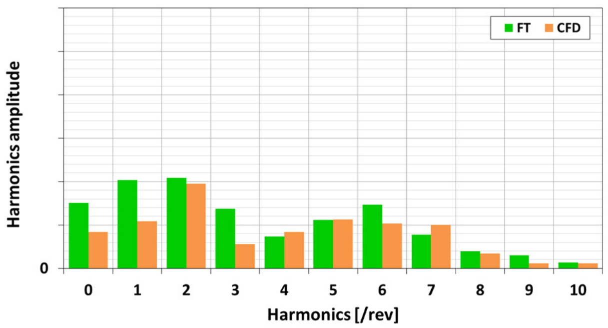

Figure 24 – Dynamic-loads harmonic decomposition (i/rev) at pitch link for TURN_1.07G_NOTAB

5.2.2 Coordinated 1.3G turn: blade modification effects

This case represents a coordinated right turn with a banking angle of approximately 40° initiated from cruise conditions at 140kt.

The three blade versions have been simulated in the same flight conditions in order to segregate the effects of the modifications, namely the tab inclusion and the mass distribution effects. For this reason and for the sake of clarity only the last iteration of the blade (using a modified mass distribution and including -8° tabs) is directly compared to flight data.

The blade without tabs posed a challenge to simulate, no flight data was available as this point was outside the flight envelope but it was included in order to compare the behaviour to the other blades. As a result, the trim targets for this case were found to be unattainable. The evolution of the pitch attitude resulting from the imposed thrust target is presented in Figure 25. In order to attain the trim target, CAMRADII tends to aggressively increase the pitch attitude probably missing the rotor stalled conditions at such high angles; this causes the trimmed pitching angle to overshoot. The CFD simulations fail to attain the trim targets at such high pitching angles where the rotor is effectively stalled and correct the loads seen by CAMRADII which in turn demands higher pitch attitudes to compensate the lack of thrust. This is illustrated in Figure 26 where the retreating side of the rotor is fully stalled for trim iteration #11. This diverging loop must be manually broken by reducing the thrust target in order to attain reasonable pitch attitudes for which the CFD simulations were capable to attain the thrust objectives. The final thrust target for which the simulations converged corresponded to a 1.21g turn (corresponding to a thrust target reduction of 600 daN) instead of the target of 1.3g. Under-relaxation of trimmed pitch could eventually be used in the future in order to mitigate the overshoot.

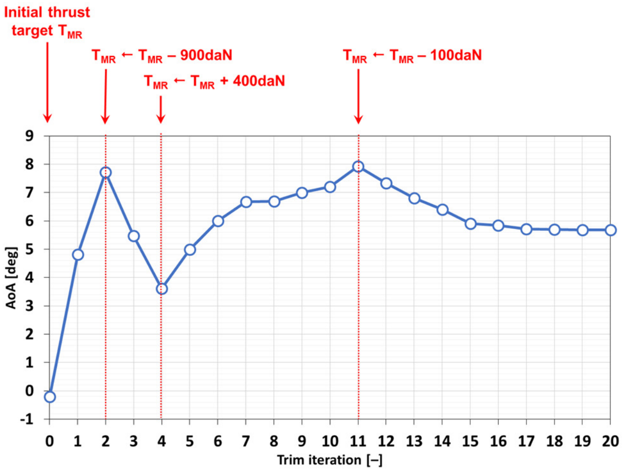

Figure 25 – Rotor Pitch history and thrust tuning

The complete trimmed quantities for the three cases are presented in Table 7 along with the flight data for the serial blade with tabs.

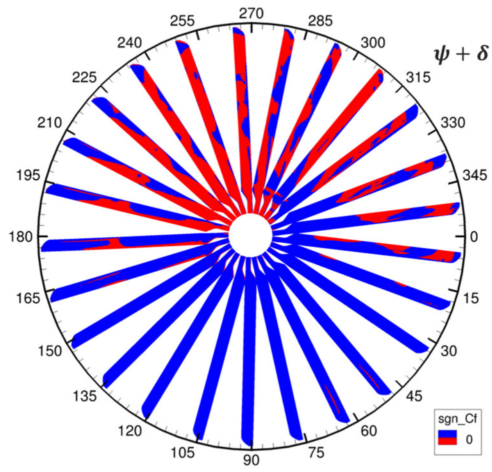

Figure 26 – Sign of the friction coefficient (blue: attached flow; red: separated flow) at the blade suction side as a function of the blade azimuth ψ for TURN_1.3G_NOTAB at trim iteration 11; δ is the blade lead lag angle

Variable	Simulation			Flight Data
	NOTAB	REF_BSL	REF_SER	REF_SER
NZ	1.21g	1.3g	1.3g	1.3g
COLL	4.14°	4.49°	4.85°	5.52°
LNGCYC	-9.61°	-7.23°	-7.72°	-6.80°
LATCYC	1.16°	1.61°	2.11°	0.38°
AoA	5.71°	5.41°	5.28°	4.41°

Table 7 – Trim control angles for the 1.3g coordinated turns

Control angles of the flight test have been reconstructed from the servo actuator lengths measurements. The offset in the longitudinal cyclic from the simulated value (case REF_SER) might be partially explained by the not-simulated pitch rate *q*, as discussed in section 4.1. However, in this context, the incidence of the no-feathering plane should also be considered, which is -6.94° (CFD) and -6.89° (FT) and thus relativizes largely the interpretation. The AoA value has been obtained from a wind vane on the nose boom, and is corrected for local vertical speed due to the pitch rate.

The pitch-link loads and their harmonic components are presented in Figure 27 and Figure 28 with respect to flight data. Overall a reasonable agreement is found albeit with an underprediction of the 1/rev loads. It should be noted that all the collective angles were found with a previous cruise trim and are thus slightly different to those found in flight. An alternative approach might consider imposing directly the in-flight measured collective angle. The flight data shows a higher harmonic content, especially for 5/rev and 7/rev components.

The peak-to-peak values are over predicted as a result of an overshoot of the peak at 10°. Nevertheless the double peak at 315° and 20° characteristic of the dynamic stall seems to be well captured.

The elastic torsion and sectional pitching moments are presented as well in Figure 29 and Figure 30 respectively, using the same scale as the results presented for the high-load cruise described in section 5.1.2. The effect of the tab (set at -8°) is clearly shown, with a strong pitching moment contribution on the full revolution which masks the stall effects. However similar aeroelastic behaviour as the flight case in high-load cruise is observed.

The pitch-link loads comparisons between the blade variants are presented in Figure 31 and Figure 32. It is reminded that the blade without tabs is computed at a lower load factor than the other ones (given the aforementioned difficulties to obtain the target thrust for this case).

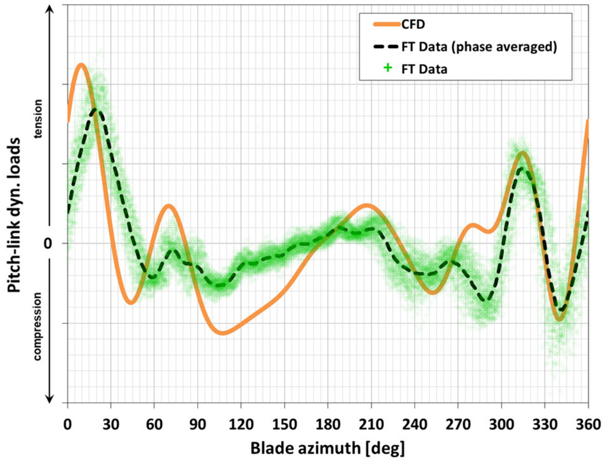

Figure 27 – Dynamic loads at pitch link as a function of the blade azimuth ψ for TURN_1.3G_REF_SER

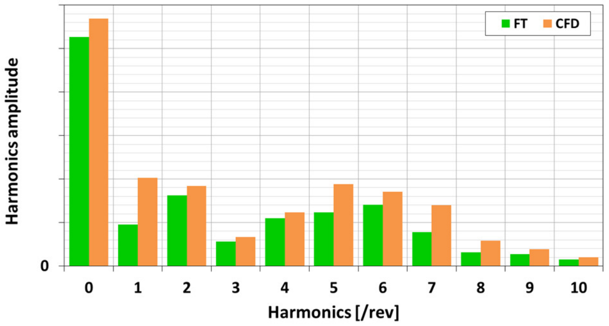

Figure 28 – Dynamic-loads harmonic decomposition (*i*/rev) at pitch link for TURN_1.3G_REF_SER

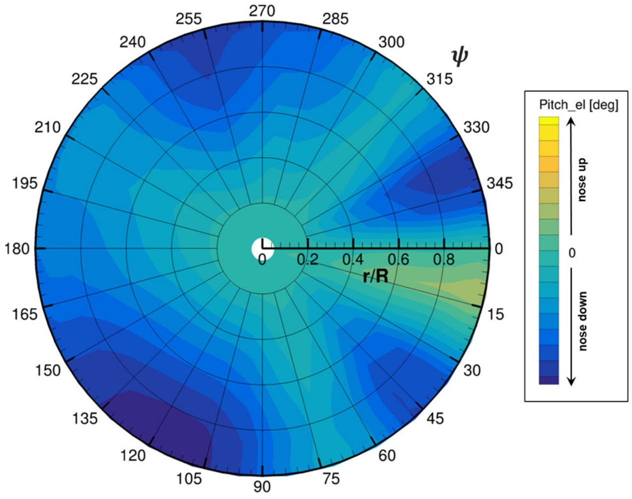

Figure 29 – Blade elastic pitch angle as a function of the blade azimuth ψ for TURN_1.3G_REF_SER

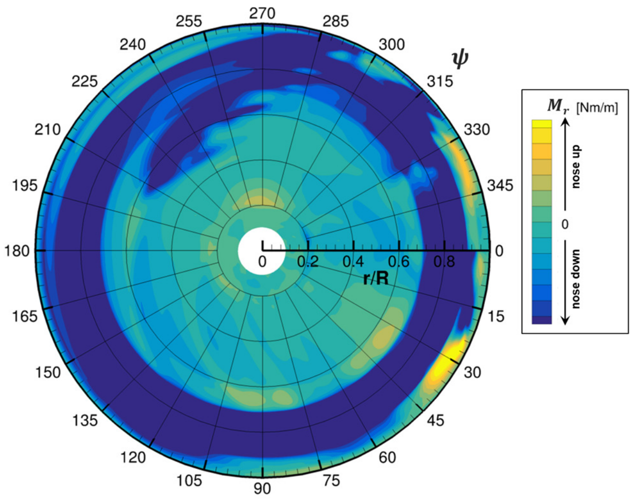

Figure 30 – Sectional pitching moment at the blade pitch axis as a function of the blade azimuth *ψ* for TURN_1.3G_REF_SER

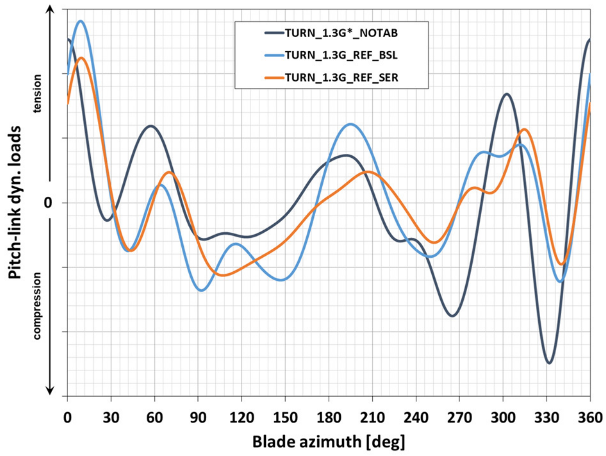

Figure 31 – Dynamic loads at pitch link as a function of the blade azimuth ψ for 1.21g (referred to as 1.3g*) & 1.3g turn simulations

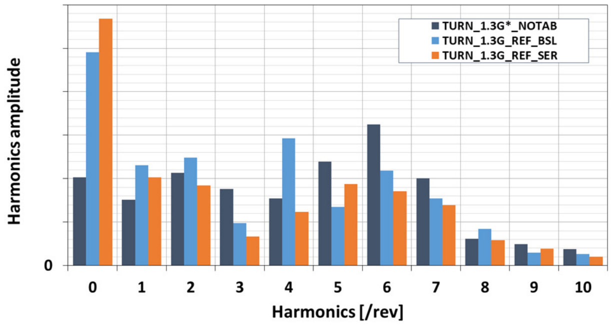

Figure 32 – Dynamic-loads harmonic decomposition (*i*/rev) at pitch link for 1.21g (referred to as 1.3g*) & 1.3g turn simulations

Nevertheless, the dynamic content on the pitch-link loads for the blade without tabs shows that the rotor is already near its limit, with greater peak-to-peak values and higher harmonic content at a significantly lower load factor than its counterparts.

Each iteration of the blade (chronologically blade without tabs and baseline structure, blade with tabs and baseline structure and blade with tabs and serial structure) shows an improved behavior over its predecessor, a good testimony of the design decisions taken during the flight campaigns, which demonstrated the same trends for the three blades.

The serial-version mass distribution contributes to lower the harmonic content of the pitch-link loads, via the modification of the blade third flapping mode.

All the presented cases in this section show signs of dynamic stall onset as described in the literature. Albeit imperfectly reproducing the flight data, the proposed simulation approach seems to capture the main phenomena at play and shows good agreement with the magnitude of pitch-link loads in absolute value as well as relative to other blade variants.

6. CONCLUSIONS

In the present work, the five-bladed H175 rotor was simulated in multiple challenging flight conditions with the main objective of reproducing flight-test blade and pitch-link loads. The chosen CFD/CSD loose coupling strategy considers a 3DoF isolated rotor but the trim targets are obtained by an initial 6DoF trim tuned with information from flight data and performed with Airbus Helicopter's in-house comprehensive code HOST.

This approach allows to better reproduce the flight-test data for a better comprehension of the physical phenomena at play thanks to the wealth of information produced by the simulations. Additionally, once a flight test data point is reasonably reproduced, it allows to numerically evaluate incremental blade evolutions based on the same conditions. This approach has been validated in this work, the toolchain allows the evaluation of tab effects as well as internal structure evolutions in challenging flight cases.

The high-altitude cruise and the coordinated turns at 1.3g cases show the hallmarks of dynamic stall phenomena, the main stall events in the 3rd rotor quadrant seem to be reasonably well captured by the simulations and is coherent with the results presented in the literature for similar flight cases. The absolute pitch-link load levels are correctly predicted including the peak-to-peak values, and the torsion moments are in good agreement with the flight data of the strain gauges.

The results show the current maturity of the simulation tools at Airbus Helicopters and paves the way for a better understanding of available flight data and to identify the shortcomings of the tools in fully predictive mode when no flight data is available.

ACKNOWLEDGEMENTS

This work was supported by CHAllenge AeRo-thermo-MEchanique (CHARME) Projects, partially funded by Direction Générale de l'Aviation Civile (DGAC). The authors are grateful for the support from Oliver Dieterich, Paul Cranga and Paul Eglin.

COPYRIGHT STATEMENTS

The authors confirm that they, and/or their company or organization, hold copyright on all of the original material included in this paper. The authors also confirm that they have obtained permission, from the copyright holder of any third party material included in this paper, to publish it as part of their paper. The authors confirm that they give permission, or have obtained permission from the copyright holder of this paper, for the publication and distribution of this paper as part of the ERF proceedings or as individual offprints from the proceedings and for inclusion in a freely accessible web-based repository.

ABBREVIATIONS

AH	Airbus Helicopters
CFD	Computational Fluid Dynamics
CSD	Computational Structure Dynamics
CHARME	CHallenge AéRoMEchanique
DoF	Degrees of Freedom
ISA	International Standard Atmosphere
FD	Flight Dynamics
FM	Flight Mechanics
FT	Flight Test
RANS	Reynolds Averaged Navier Stokes
URANS	Unsteady Reynolds Averaged Navier Stokes

SYMBOLS

AoA	Rotor angle of attack	[°]
COLL	Main rotor collective pitch	[°]
$\mathrm{COLL_{TR}}$	Tail rotor collective pitch	[°]
$\mathrm{D_{Fus}}$	Airframe drag force	[N]
$\mathrm{F_X}$	Longitudinal rotor disk in-plane force	[N]
$\mathrm{F_Y}$	Lateral rotor disk in-plane force	[N]
g	Gravity at Earth surface	[m/s²]
ΔISA	Temperature shift from ISA	[°C]
LATCYC	Blade lateral cyclic pitch	[°]
LNGCYC	Blade longitudinal cyclic pitch	[°]
N	Load factor w.r.t. gravity (g)	[%g]
NR	Rotor rotational speed w.r.t. nominal speed	[%]
q	Roll rate	[rad/s]
R	Rotor radius	[m]
TAS	True Air speed	[kt]
$\mathrm{T_{MR}}$	Main rotor thrust	[N]
$\mathrm{V_H}$	Horizontal velocity	[m/s]
$\mathrm{V_Z}$	Vertical velocity	[m/s]
$\mathrm{Z_p}$	Pressure altitude	[ft]
α	Shaft incidence angle	[°]
β_{1c}	Longitudinal flapping angle	[°]
β_{1s}	Lateral flapping angle	[°]
δ	Blade lead-lag angle	[°]
τ	Slope angle $\tau = \tan^{-1}\left({}^{V_z}/_{V_H}\right)$	[°]
Θ	Helicopter pitch attitude	[°]
${}^{\mu_t}/_{\mu}$	Turbulent viscosity ratio	[–]
Φ	Helicopter roll angle	[°]
Ψ	Helicopter yaw angle	[°]
ψ	Azimuth of the rotor reference blade	[°]

REFERENCES

[1] **Kufeld, R. M., Balough, D. L., Cross, J. L., Studebaker, K. F., Jennison, C. D. & Bousman, W. G.,** *Flight Testing the UH-60A Airloads Aircraft*, American Helicopter Society International Annual Forum and Technology Display,Washington, DC,1994.

[2] **Bousman, W.,** *A Qualitative Examination of the Dynamic Stall from Flight Test Data*, 53rd AHS Annual Forum, Virginia Beach, VA, USA, May 1997.

[3] **Potsdam, M., Yeo, H., & Johnson, W.,** *Rotor Airloads Prediction Using Loose Aerodynamic/Structural Coupling*, Journal of Aircraft, Vol. 43, No. 3, May-June 2006, pp. 732-742.

[4] **Ortun, B., Potsdam, M., Yeo, H., Van Truong, K.,** *Rotor Loads Prediction on the ONERA 7A Rotor Using Loose Fluid/Structure Coupling*, Journal of the American Helicopter Society, Volume 62, Number 3, July 2017, pp. 1-13(13).

[5] **Richez, F.,** *Analysis of Dynamic Stall Mechanisms in Helicopter Rotor Environment*, Journal of the American Helicopter Society, Volume 63, (3), 2018, pp. 1-11.

[6] **Castells, C., Richez, F. & Costes, M.,** *A numerical analysis of the dynamic stall mechanisms on a helicopter rotor from light to deep Stall*, J. of American Helicopter Society, 65 (3), 2020.

[7] **Kowarsch, U., Öhrle, C., Keßler, M. & Krämer, E.,** *Aeroacoustic simulation of a complete H145 helicopter in descent flight*, J. of American Helicopter Society, 61 (4), 2016.

[8] **Letzgus, J., Keßler, M. & Krämer, E,** *Simulation of Dynamic Stall on an Elastic Rotor in High-Speed Turn Flight*, Journal of the American Helicopter Society, Volume 65, Number 2, April 2020, pp. 1-12(12).

[9] **Bebesel, M., D'Alascio, A., Schneider, S., Guenther, S., Vogel, F., Wehle, C., & Schimke, D.,** *Bluecopter Demonstrator – An Approach to eco-efficient helicopter design*, Proceedings of the 41th European Rotorcraft Forum, Munich, Germany, September 1–4, 2015.

[10] **Kroll, N., Eisfeld, B. & Bleeke, H.,** *The Navier-Stokes code FLOWer*, Notes on Numerical Fluid Mechanics, vol. 71, pp. 58-71, 1999.

[11] **Johnson, W.,** *Technology drivers in the development of CAMRADII,* AHS Conference, San Francisco, California, 1994.

[12] **Benoit, B., Dequin, A.M., Kampa, K., VonGrünhagen W., Basser P.M. & Gimonet, B.,** *HOST, a general helicopter simulation tool for Germany and France*, 56th Annual Forum of the American Helicopter Society, Virginia Beach, USA, 2000.

[13] **Vuillet, A., Allongue, M. Philippe, J.J. & Desopper, A.** *Performance and aerodynamic development of the Super Puma Mk2 main rotor with new SPP8 blade tip design*, 15th congrès sur les hélicoptères, ONERA TP n° 1989-181 (1989).

[14] **Keßler, M., Frey, F., Letzgus, J., Öhrle, C., Thiemeier, J. & Krämer, E.,** *Progress in IAG's rotorcraft simulation framework*, High performance computing in science and engineering '20, Springer edition, 2021.

[15] **Benek, J.A., Steger, J.L., Doughety, F.C. & Buning, P.G.,** *Chimera: a grid-embedding technique*, AEDC technical report 85-64, 1986.

[16] **Menter, F.R.,** *Two-equation eddy viscosity turbulence model for engineering applications,* AIAA J. Vol 32, 8, pp. 1598-1605, 1994.

[17] **Jameson, A.J.,** *Time dependent calculation using multigrid, with application to unsteady flow past airfoils and wings,* AIAA paper 91-1596, 1991.

Presented at 48th European Rotorcraft Forum, Winterthur, Switzerland, 6-8 September, 2022